



# Synthesis and characterization of hollow spherical cathode $\text{Li}_{1.2}\text{Mn}_{0.54}\text{Ni}_{0.13}\text{Co}_{0.13}\text{O}_2$ assembled with nanostructured particles via homogeneous precipitation-hydrothermal synthesis

Feng Wu<sup>a, c</sup>, Zhao Wang<sup>a</sup>, Yuefeng Su<sup>a, c, \*</sup>, Yibiao Guan<sup>b</sup>, Yi Jin<sup>b</sup>, Na Yan<sup>a</sup>, Jun Tian<sup>a</sup>, Liying Bao<sup>a, c</sup>, Shi Chen<sup>a, c</sup>

<sup>a</sup> School of Chemical Engineering and Environment, Beijing Institute of Technology, Beijing Key Laboratory of Environmental Science and Engineering, Beijing 100081, China

<sup>b</sup> China Electric Power Research Institute, Beijing 100192, China

<sup>c</sup> National Development Center of High Technology Green Materials, Beijing 100081, China

## H I G H L I G H T S

- Two different kind of hollow spherical materials were successfully prepared.
- HP-PVP sample exhibits a better structural stability and a weaker voltage drop.
- HP-PVP sample exhibits a high capacity of  $240.9 \text{ mAh g}^{-1}$  after 50 cycles.
- A high capacity  $170.5 \text{ mAh g}^{-1}$  of HP-PVP is obtained after 112 cycles at 1.0 C.

## A R T I C L E I N F O

### Article history:

Received 28 January 2014

Received in revised form

18 May 2014

Accepted 20 May 2014

Available online 29 May 2014

### Keywords:

Lithium ion battery

Layered structure

Hollow spherical

Nanoplate

Cathode material

## A B S T R A C T

Two different kinds of hollow spherical materials  $\text{Li}_{1.2}\text{Mn}_{0.54}\text{Ni}_{0.13}\text{Co}_{0.13}\text{O}_2$  which are assembled by the nanoplate-shaped particles and the quasi-sphere shaped particles, have been prepared through the homogeneous precipitation of metal oxalate precursor and subsequent solid state reaction with lithium nitrate. X-ray diffraction (XRD) pattern shows the two as-prepared samples have a good layered structure and solid solution characteristic. As the lithium-ion battery cathode, the as-prepared sample exhibits an initial discharge capacity of  $286.4 \text{ mAh g}^{-1}$  at 0.1 C between 2.0 and 4.8 V, and a discharge capacity of  $240.9 \text{ mAh g}^{-1}$  can be retained after 50 cycles. The structure of hollow spherical material is assembled with nanoplate-shaped particles, which is beneficial for improving the rate performance. It is due to the shortened transmission distance for  $\text{Li}^+$  from the cathode materials to electrolyte. At the charge–discharge rate of 1.0 C, a stable discharge capacity of  $170.5 \text{ mAh g}^{-1}$  also can be reached after 112 cycles with capacity retention of 86.2%. Meanwhile, the relationship of structure and electrochemical performance is also discussed in detail.

© 2014 Elsevier B.V. All rights reserved.

## 1. Introduction

A lithium ion battery (LIB) with excellent electrochemical performance attracts high level of attention and extensive research since its advent [1,2]. A large variety of materials have been synthesized and evaluated as cathode materials for LIBs, such as  $\text{LiCoO}_2$

[3],  $\text{LiNiO}_2$  [4],  $\text{LiMnO}_2$  [5],  $\text{LiMn}_2\text{O}_4$  [6],  $\text{LiFePO}_4$  [7], and  $\text{LiNi}_{1-x}\text{Co}_x\text{Mn}_2\text{O}_2$  [8]. However, their unsatisfied capacities (below  $200 \text{ mAh g}^{-1}$ ) and low conductivity of electrons and lithium ions restrict their development and commercial applications in lithium ion batteries.

In recent years, composite layered cathode materials  $x\text{Li}_2\text{MnO}_3 \cdot (1-x)\text{LiMO}_2$  ( $\text{M} = \text{Ni, Co, Fe, Ni}_{1/2}\text{Mn}_{1/2}, \text{Ni}_{1/3}\text{Mn}_{1/3}\text{Co}_{1/3} \dots$ ), which can be regarded as the solid solution of  $\text{Li}_2\text{MnO}_3$  and  $\text{LiMO}_2$ , have received widespread attention. Because of their advantages of high specific capacity (over  $250 \text{ mAh g}^{-1}$ ), good cycle and thermal stability, wide charge–discharge potential range, low cost and environmental friendliness, such cathode materials are

\* Corresponding author. School of Chemical Engineering and Environment, Beijing Institute of Technology, Beijing Key Laboratory of Environmental Science and Engineering, Beijing 100081, China. Tel.: +86 10 6891 8099; fax: +86 10 6891 8200.  
E-mail address: [suyuefeng@bit.edu.cn](mailto:suyuefeng@bit.edu.cn) (Y. Su).

considered to be of great potential as a new generation of positive electrode materials for high energy density lithium ion batteries [9–17].

Several methods have been used to synthesis solid solution cathode materials  $x\text{Li}_2\text{MnO}_3 \cdot (1-x)\text{LiMO}_2$ , such as co-precipitation method [9], sol–gel method [10], spray drying method [11], sucrose-combustion method [12], solid solution method [13], molten salt method [14], template-free method [15], microwave heating process [16], and lithium ion-exchange reaction [17]. Among these methods, the widely used one is the co-precipitation method, which can give phase-pure products with uniform and smaller particle size. However this method cannot avoid the space and time difference in the precipitation process of transition metal ions. Homogeneous precipitation-hydrothermal synthesis [18,19] is a modified precipitation method, which can effectively overcome this disadvantage. During the homogeneous precipitation, the precipitating agent is slowly formed in the reaction mixture, allowing ripening of particles during precipitation and often resulting in better crystallinity, regular shape and size of particles.

As we all know, the morphology and structure have great influence on the electrochemical performances of cathode materials. Spherical materials have excellent liquidity, dispersion and processing performances. It is very beneficial to making the slurry and the coated electrodes of the cathode material. In addition, relative to the irregular particles, the regular spherical particles are advantageous to the uniform surface modification which can further improve the electrochemical performances. For example, it is easier to coat a complete and uniform coating layer [20–22] on the surface of the regular spherical particles. Therefore, spherical cathode material is one of the important development directions. However, for the solid spherical materials, the electrolyte cannot infiltrate into the active materials very well, especially into the dense internal accumulation. This limits the deintercalation/intercalation of  $\text{Li}^+$  from/into the inner part of the solid spherical materials quickly, which leads to the low utilization rate and the poor rate performance of the active materials. Ideally, the hollow sphere materials assembled with nanostructured particles are promising to solve this problem. It is due to the shorter path for the deintercalation/intercalation of  $\text{Li}^+$  ( $\text{Li}^+$  can be away from/into the cathode materials through both outer and inner surfaces of the shell).

In this paper, we reported the successful synthesis of the hollow spherical materials  $\text{Li}_{1.2}\text{Mn}_{0.54}\text{Ni}_{0.13}\text{Co}_{0.13}\text{O}_2$  ( $0.5\text{Li}_2\text{MnO}_3 \cdot 0.5\text{LiNi}_{1/3}\text{Co}_{1/3}\text{Mn}_{1/3}\text{O}_2$ ) using PVP as structure-directing agent, which assembled by the nanoplate-shaped particles by homogeneous precipitation-hydrothermal synthesis (hereinafter referred to HP-PVP). For comparison, the hollow spherical materials without PVP as structure-directing agent, which assembled by the nanoparticles were also prepared (hereinafter referred to HP). HP-PVP sample exhibits good rate and cycle performances ( $183.9 \text{ mAh g}^{-1}$  @ 1.0 C,  $205.8 \text{ mAh g}^{-1}$  @ 2.0 C, and retention of 86.2% after 112 cycles @ 1.0 C). Compared with other research results, HP-PVP exhibits a higher discharge capacity [22,23] and a better cycling ability [20,24]. In addition, their relationship of structure and electrochemical performance was also investigated in detail.

## 2. Experimental

### 2.1. Preparation of HP and HP-PVP samples

The HP-PVP sample was synthesized according to the steps below. The starting materials  $\text{Mn}(\text{CH}_3\text{COO})_2 \cdot 4\text{H}_2\text{O}$ ,  $\text{Ni}(\text{CH}_3\text{COO})_2 \cdot 4\text{H}_2\text{O}$ , and  $\text{Co}(\text{CH}_3\text{COO})_2 \cdot 4\text{H}_2\text{O}$  were weighed with the

stoichiometry of Mn:Ni:Co as 54:13:13 and made into a transparent and homogeneous solution in a mixture solvent of ethylene glycol and distilled water with the volume ratio of 1:1. Polyvinylpyrrolidone (PVP) used as structure-directing agent was added to the above solution with continuous stirring. After the stoichiometric dimethyl oxalate (DMO) added to the solution, the mixture solution was then stirred for 30 min until a transparent and homogeneous solution was obtained at room temperature. The prepared solution was poured into a 100 ml Teflon-lined stainless reactor with the volume filling ratio of 80%. Afterward the reactor was tightened and heated in an air-circulating oven at  $200^\circ\text{C}$  for 12 h, and then cooled down to room temperature naturally. The products were washed with deionized water and ethanol 3 times, respectively. Finally, they were dried in the vacuum oven at  $80^\circ\text{C}$  for 5 h. The dried precursors were collected and mixed with  $\text{LiNO}_3$  in the molar ratio of 1:1.26 and then preliminarily fired at  $450^\circ\text{C}$  for 5 h in air. Afterward, the obtained materials were ground uniformly and subjected to further heat treatment at  $900^\circ\text{C}$  for 12 h. The final product was obtained by grinding up and sifting through 200 mesh screen. The synthetic steps of HP sample were identical to that of HP-PVP sample, except that PVP was not added as structure-directing agent. For comparing and analyzing the influence of morphology and structure on the electrochemical performances, the samples with granular (hereinafter referred to P) and solid spherical shape (hereinafter referred to SS) were also synthesized. P sample was synthesized by co-precipitation method using ammonium oxalate as precipitant. The synthetic steps of SS sample were identical to that of HP sample, except that the solvent is only distilled water.

### 2.2. Sample characterization

The powder X-ray diffraction patterns of as-prepared samples were measured using an X-ray diffractometer (XRD, Ultima IV-185, Rigaku, Japan) with Cu K $\alpha$  radiation at a scanning rate of  $8^\circ \text{ min}^{-1}$  in the  $2\theta$  range from  $10^\circ$  to  $90^\circ$  to characterize the crystal structures of the synthesized materials. The surface morphology and element energy spectrum (EDX) were observed using a Field emission scanning electron microscope (FESEM, QUANTA 250, FEI, USA). Specific area test was performed on Autosorb-iQ (QUANTACHROME, USA).

### 2.3. Electrochemical tests

Electrochemical properties of the HP and HP-PVP electrodes were measured by assembling them into coin cells (type CR2025) in an argon-filled glove box. The cathode was prepared by spreading a mixture of 80 wt% active material, 10 wt% conductive additive acetylene black, and 10 wt% binder PVDF onto a smooth Al foil current collector. The obtained electrodes were dried at  $120^\circ\text{C}$  for 24 h in a vacuum oven. The coated foil was roll pressed to well adhere the material to the current collector. Lithium foil was used as the negative electrode and Celgard 2400 membrane was used as the separator. The electrolyte was 1 M  $\text{LiPF}_6$  dissolved in a mixture of ethylene carbonate (EC) and dimethyl carbonate (DMC) with volume ratio of 1:1. Galvanostatic charge–discharge cycling test was performed at room temperature in the voltage range of 2.0–4.8 V using Land battery test system (Wuhan, China). The rate capability of the electrode materials was also tested between 2.0 and 4.8 V by charging at 0.1 C and discharging at different rates. EIS data were collected with AC amplitude of 10 mV in the frequency range of 100 kHz to 1 mHz by a CHI604D Electrochemical Station (Shanghai, China). A 1 C rate is equivalent to  $250 \text{ mA g}^{-1}$  in our definition. The potentials throughout the paper are referenced to the Li/Li $^+$  couple.

### 3. Results and discussion

#### 3.1. Structure of the samples

The XRD patterns of the as-prepared solid solution  $0.5\text{Li}_2\text{MnO}_3 \cdot 0.5\text{LiNi}_{1/3}\text{Co}_{1/3}\text{Mn}_{1/3}\text{O}_2$  powders (HP and HP-PVP) synthesized by homogeneous precipitation-hydrothermal process are shown in Fig. 1, respectively. It can be seen that these peaks are characteristic of a complex  $\text{Li}_2\text{MnO}_3$ – $\text{LiMO}_2$  phase, resulting from the ordering of metal ions (Li, Ni, Co and Mn) and the existence of a  $\text{Li}_2\text{MnO}_3$  phase. No peak for any impurity phase is detected in the patterns, indicating the high purity of the as-synthesized oxides. All of the diffraction peaks can be indexed based on a layered hexagonal  $\alpha$ - $\text{NaFeO}_2$  structure with a space group of  $R\bar{3}m$ , and the peaks are very sharp which indicates the good crystallinity of the as-prepared samples.

Furthermore, a few weak super lattice reflections peaks presented between  $20^\circ$  and  $25^\circ$  (blue box in Fig. 1) are known to be caused by the super lattice ordering of  $\text{Li}^+$  and  $\text{Mn}^{4+}$  in the transition metal layers for the layered  $\text{Li}_2\text{MnO}_3$  ( $\text{Li}[\text{Li}_{1/3}\text{Mn}_{2/3}]\text{O}_2$ ), which can be ascribed to the monoclinic phase with a space group of  $C/2m$  [25,26]. Another observation in the XRD patterns is the clear separation of the (006)/(012) and (018)/(110) peaks (blue box (in the web version only) in Fig. 1), which indicates the formation of a well-crystallized layered structure [27].

The lattice parameter ( $a$  and  $c$ ), the  $c/a$  values, the  $I(003)/I(104)$  values, and the  $R$  [ $R = (I(006) + I(012))/I(101)$ ] values of HP and HP-PVP are furnished in Table 1. It is well documented that the  $c/a$  value can indicate the degree of trigonal distortion and thus a higher cation ordering attributed to this distortion would be achieved when  $c/a$  value is higher than 4.899 (the ideal ccp lattice constant) [28]. The  $c/a$  values for the two samples are about 4.98, which are higher than 4.899. It indicated that the two samples have a high cation ordering. The intensity ratio of (003)/(104) diffraction peaks depends on the degree of the cation disorder between  $\text{Li}^+$  and  $\text{Ni}^{2+}$ . When  $I(003)/I(104)$  is less than 1.2, undesirable cation mixing would occur in the lattice [29]. It is seen from Table 1 that the  $I(003)/I(104)$  ratio of the two samples are higher than 1.2, which indicated the low cation mixing.  $R$  factor can show the order degree of the hexagonal lattice. The  $R$  values of the two samples are all below 0.4, indicating a well-formed layered structure. Compared with the two samples, HP-PVP sample has a larger value of  $c/a$  and  $I(003)/I(104)$ , and a smaller value of  $R$  factor than HP sample, indicating a better layered structure which will probably exhibit the better electrochemical performances.

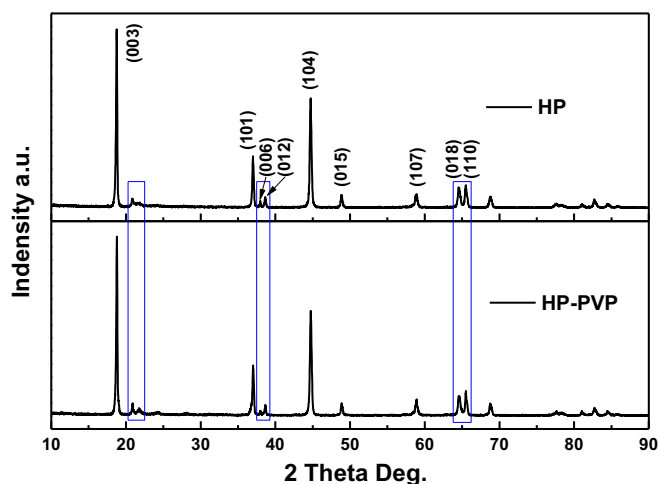


Fig. 1. The XRD patterns of the as-prepared samples.

Table 1

The lattice parameter ( $a$  and  $c$ ), the  $c/a$  values, the  $I(003)/I(104)$  values, and the  $R$  [ $R = (I(006) + I(012))/I(101)$ ] values of the as-prepared samples.

Samples	$a$ (nm)	$c$ (nm)	$c/a$ ratio	$I(003)/I(104)$	$R$ -factor
HP	0.28480	1.41874	4.9815	1.6325	0.3601
HP-PVP	0.28416	1.41742	4.9881	1.7104	0.3231

#### 3.2. Morphology of the samples

If the particle diameter of the prepared samples is too large, the electrolyte cannot infiltrate into the materials, leading to the low utilization rate and the poor rate performance. However, if the particle diameter of the prepared samples is too small, the cycle stability will get worse because of the excessive side reactions with the electrolyte and so on. Ideally, hollow spheres materials assembled with nanostructured particles are promising to reach good rate and cycle performances.

As is well-known, the morphology and structure have great influence on the electrochemical performances of lithium cathode materials. Fig. 2 shows the SEM images of the two as-prepared samples. It can be seen that two as-prepared samples have a hollow spherical morphology with a shell thickness of approximately  $1.7\text{ }\mu\text{m}$ . Compared with the solid spherical cathode material, hollow spherical shaped cathode material has many advantages such as larger specific surface area, higher specific power densities and shorter transport path for  $\text{Li}^+$ .

As shown in Fig. 2, the shape of the small particles of the two as-prepared hollow spherical samples is different. Sample HP is composed of relatively homogenous quasi-sphere shaped particles with the dimensions in the range of  $200\text{--}400\text{ nm}$ . The particles of HP are agglomerated much closer, and the shell thickness of HP is about  $1.869\text{ }\mu\text{m}$ . Unlike HP, HP-PVP is comprised of nanoplate-shaped particles. The shell thickness of hollow sphere is about  $1.639\text{ }\mu\text{m}$ , and the thickness of nanoplate-shaped particle is about  $150\text{ nm}$ . These morphological differences can affect the contact area with the electrolyte, which association with the rate performances of the cathode materials. The main reason of the difference above is the use of PVP which serves as structure-directing agent in the precipitation process.

In addition, EDX spectroscopy was used to verify the distribution of the transition metals (Mn, Ni, Co) in the as-prepared samples. The EDX analysis results are shown in Fig. 3. As can be seen in Fig. 3(a–d), all three transition metals (Mn, Ni, Co) in the as-prepared samples are well distributed and no obvious clustering is observed. Fig. 3(e) and (f) shows a comparison of the theoretical stoichiometry values and the calculated molar ratios of Mn, Ni, and Co for the as-prepared samples. It can be found that the calculated molecular formulas of HP ( $\text{Li}_{1.191}\text{Mn}_{0.54}\text{Ni}_{0.131}\text{Co}_{0.128}\text{O}_2$ ), HP-PVP ( $\text{Li}_{1.192}\text{Mn}_{0.54}\text{Ni}_{0.13}\text{Co}_{0.129}\text{O}_2$ ), P ( $\text{Li}_{1.188}\text{Mn}_{0.54}\text{Ni}_{0.132}\text{Co}_{0.128}\text{O}_2$ ) and SS ( $\text{Li}_{1.191}\text{Mn}_{0.54}\text{Ni}_{0.131}\text{Co}_{0.128}\text{O}_2$ ) samples are approximately the same as the theoretical one ( $\text{Li}_{1.2}\text{Mn}_{0.54}\text{Ni}_{0.13}\text{Co}_{0.13}\text{O}_2$ ). It means that the as-prepared samples are synthesized with good stoichiometry.

As shown in Fig. 4, the synthesis can be approximately divided into five stages: (1) dimethyl oxalate (DMO) uniformly dispersed in the reaction solution gradually decomposes, (2) crystal nucleus of transitional metal precipitation with oxalate is generated in the water phase, (3) PVP used as structure-directing agent is absorbed to direct the formation of the  $\text{Ni}_{0.13}\text{Co}_{0.13}\text{Mn}_{0.54}(\text{C}_2\text{O}_4)_{0.8}$  precursor [30], (4) the precursor  $\text{Ni}_{0.13}\text{Co}_{0.13}\text{Mn}_{0.54}(\text{C}_2\text{O}_4)_{0.8}$  template crystals grow into nanoplates, and the nanoplates are assembled into the hollow spherical shells which are made of ethylene glycol as the core in the hydrothermal process, and (5) the lithiation process and further growth of the hollow spherical shells are achieved under



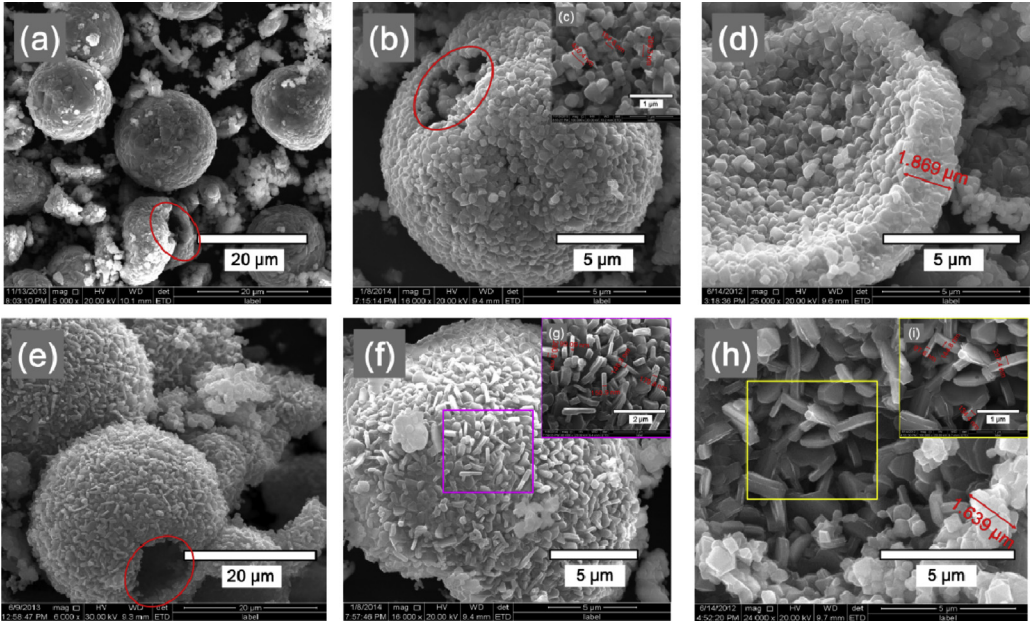


**Fig. 2.** SEM images of the as-prepared samples: (a) HP, (b) and (c) HP-outside surface, (d) HP-internal surface, (e) HP-PVP, (f) and (g) HP-PVP-outside surface, (h) and (i) HP-PVP-internal surface.

the high calcined temperature. The use of PVP makes the growth of crystals layer by layer, leading to a good layer structure of the samples [15,30–32]. The XRD test results in Fig. 1 just proved this inference. In addition, homogeneous precipitation-hydrothermal synthesis overcomes the space and time difference in the precipitation process of transition metal ions, which makes a considerable contribution to the excellent layer crystal structure.

3.3. Electrochemical properties

Fig. 5(a) and (c) shows the charge–discharge voltage profiles at different cycles of the as-prepared samples cell at a constant current density of 25 mA g<sup>−1</sup> (~0.1 C rate) between 2.0 and 4.8 V at room temperature. The initial charge capacities of HP and HP-PVP samples are 368.9 and 367.7 mAh g<sup>−1</sup>, and the discharge capacities are 277.6 and 286.4 mAh g<sup>−1</sup>, with large initial irreversible

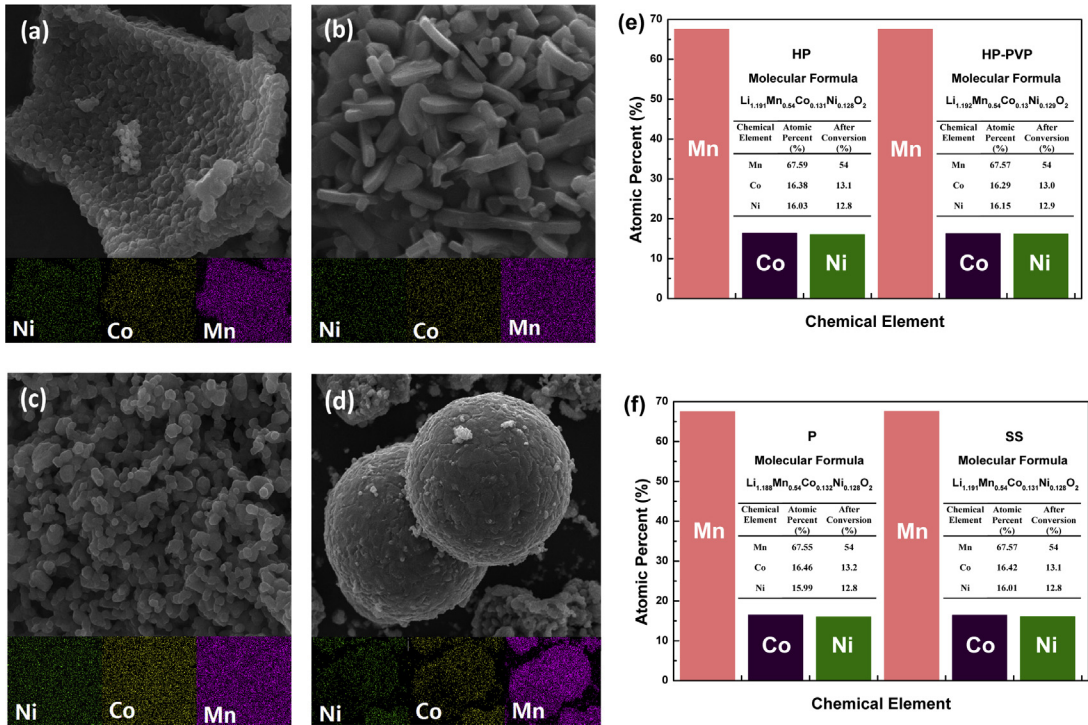


**Fig. 3.** The EDX mapping images of the as-prepared samples: (a) HP, (b) HP-PVP, (c) P, (d) SS, and (e, f) the transition metals element content of the as-prepared samples.

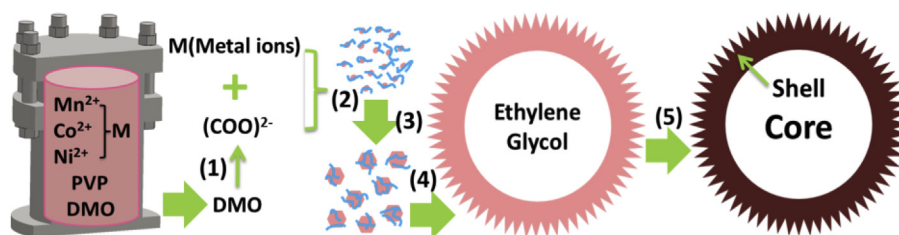
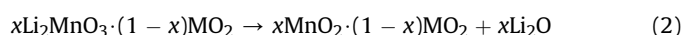


Fig. 4. The synthetic process of HP-PVP sample.

capacity of 75.4 and 77.9 mAh g<sup>-1</sup>, respectively. As seen from Fig. 5(a) and (c), both the as-prepared samples exhibit two distinguished voltage plateaus during the initial charge process: a sloping region below 4.5 V and a long plateau region above 4.5 V.



The sloping region (below 4.5 V) is attributed to the extraction of Li<sup>+</sup> from the LiNi<sub>1/3</sub>Co<sub>1/3</sub>Mn<sub>1/3</sub>O<sub>2</sub> component. At the same time, the Ni<sup>2+</sup> and Co<sup>3+</sup> are oxidized to Ni<sup>4+</sup> and Co<sup>4+</sup>, respectively. The subsequent long voltage plateau is around 4.5 V, which is beyond the formal oxidation potential of Ni<sup>2+</sup> to Ni<sup>4+</sup> and Co<sup>3+</sup> to Co<sup>4+</sup>. It is assigned to the simultaneous removal of Li<sup>+</sup> and O<sup>2-</sup> (as Li<sub>2</sub>O) from the lattice of Li<sub>2</sub>MnO<sub>3</sub> (Li[Li<sub>1/3</sub>Mn<sub>2/3</sub>]O<sub>2</sub>) component of the electrode structure [25,33,34]. The ideal two-step process during the first charge can be expressed by reactions (1) and (2). However, the

long voltage plateau above 4.5 V disappears in the second charge process. The reason is that the removal of “Li<sub>2</sub>O” from Li<sub>2</sub>MnO<sub>3</sub> component is irreversible. It is impossible to reintroduce oxygen into the structure on the subsequent discharge. It is also the main reason for the irreversible capacity loss in the initial cycle of the lithium-rich layered cathode materials [35].

The initial discharge capacities of HP and HP-PVP are 277.6 and 286.4 mAh g<sup>-1</sup>, respectively. The high discharge capacity may be due to the electrochemical activation of Li<sub>2</sub>MnO<sub>3</sub>, which makes Mn work in the subsequent cycles. During the oxygen loss plateau, the component Li<sub>2</sub>MnO<sub>3</sub> is activated to form MnO<sub>2</sub>-like component, and then the MnO<sub>2</sub>-like component is transformed into layered LiMnO<sub>2</sub> with progressive cycles [36]. Table 2 shows the theoretical discharge capacity of 0.5Li<sub>2</sub>MnO<sub>3</sub>·0.5LiNi<sub>1/3</sub>Co<sub>1/3</sub>Mn<sub>1/3</sub>O<sub>2</sub> based on the different electrochemical reaction of the transition metals. By comparison, it can thus be concluded that the electrochemical reaction in the initial discharge process is Co<sup>4+/3+</sup>, Ni<sup>4+/2+</sup> and Mn<sup>4+/3+</sup> (Mn in Li<sub>2</sub>MnO<sub>3</sub>), which confirms the analysis above. Hence, the ideal process during discharge can be expressed by reaction (3).

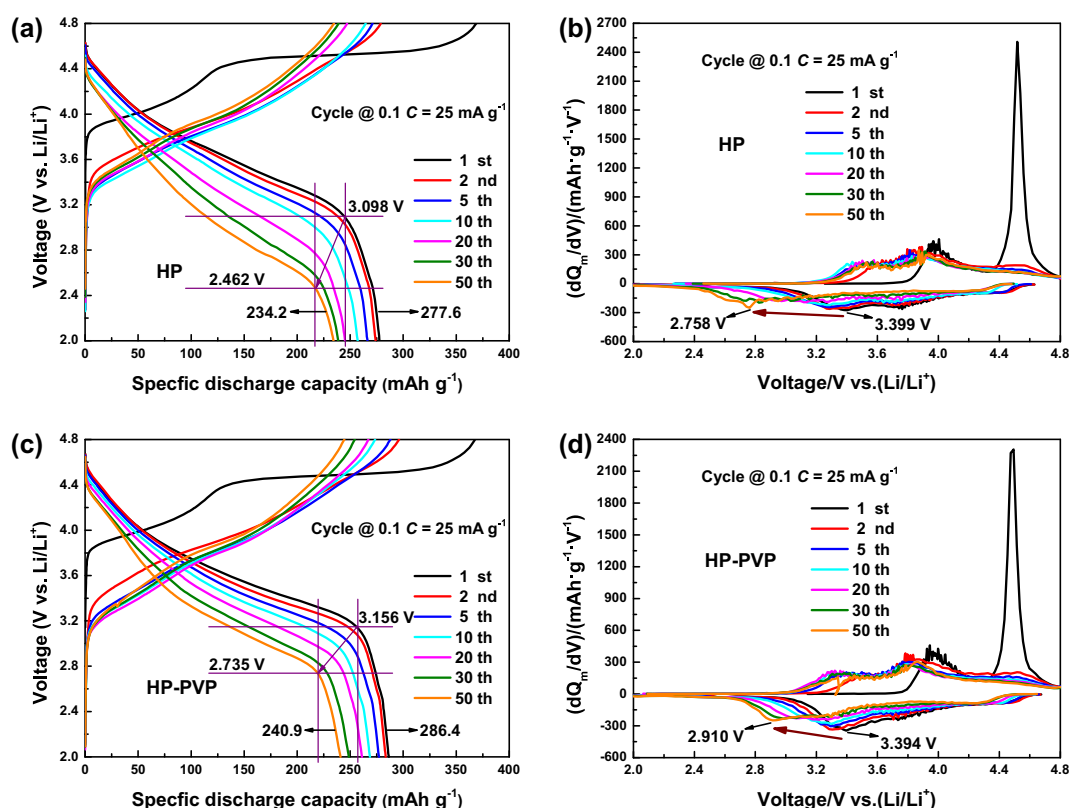


Fig. 5. The charge-discharge voltage profiles and the  $dQ_m/dV$  curves of the as-prepared samples at a constant current density of 25 mA g<sup>-1</sup> in the range from 2.0 to 4.8 V at room temperature: (a, b) HP, (c, d) HP-PVP.

**Table 2**

The theoretical discharge capacity of  $0.5\text{Li}_2\text{MnO}_3 \cdot 0.5\text{LiNi}_{1/3}\text{Co}_{1/3}\text{Mn}_{1/3}\text{O}_2$  based on the different electrochemical reaction of the transition metals.

Electrochemical reaction based on	$\text{Co}^{3+/4+}$ , $\text{Ni}^{3+/4+}$	$\text{Co}^{3+/4+}$ , $\text{Ni}^{2+/4+}$	$\text{Co}^{3+/4+}$ , $\text{Ni}^{3+/4+}$ , $\text{Mn}^{3+/4+}$ (part: in $\text{Li}_2\text{MnO}_3$ )	$\text{Co}^{3+/4+}$ , $\text{Ni}^{2+/4+}$ , $\text{Mn}^{3+/4+}$ (part: in $\text{Li}_2\text{MnO}_3$ )
Theoretical discharge capacity	83.8	125.7	209.4	251.3

As shown in Fig. 5(a) and (c), with successive cycles the discharge profiles of HP and HP-PVP move to lower voltage plateaus, showing significant loss of energy and capacity. The origin of such rapid drop in the discharge voltage profile could be associated with the gradual structure change of the cathode material from the layered structure to a spinel-like structure. As reported by Thackeray [37], high crystallinity is essential to obtain good electrochemical properties and to maintain its structural integrity during cycling. Thus, this behavior implies that for  $0.5\text{Li}_2\text{MnO}_3 \cdot 0.5\text{LiNi}_{1/3}\text{Co}_{1/3}\text{Mn}_{1/3}\text{O}_2$  electrode, the good primal layered structure can suppress the structural degradation during the cycling process. As discussed above (Fig. 1 and Table 1), HP-PVP sample has a better layered structure than HP sample, indicating HP-PVP sample will probably exhibit the better electrochemical performances. Compared with HP sample, HP-PVP sample has a slower drop in the discharge voltage profile, which indicates less structural transformations happened in the continuous cycling processes.

Fig. 5(b), (d) and Fig. 6 present the differential specific gravimetric capacity vs. voltage ( $dQ_m/dV$ ) curves. Similarly, there are two obvious oxidation peaks at 4.0 V and 4.5 V respectively in the initial charge process. A small oxidation peak at around 4.0 V, corresponding to the voltage slope at voltage <4.5 V in Fig. 5(a) and (c), is due to the  $\text{Li}^+$  deintercalation from the  $\text{LiNi}_{1/3}\text{Mn}_{1/3}\text{Co}_{1/3}\text{O}_2$  component accompanied with the oxidation of transition metals  $\text{Ni}^{2+}$  to  $\text{Ni}^{4+}$  and  $\text{Co}^{3+}$  to  $\text{Co}^{4+}$ .

The sharp oxidation peaks at around 4.5 V in the initial charge are also observed corresponding to the voltage plateau at around 4.5 V shown in Fig. 5(a) and (c), attributed to the further lithium deintercalation and oxygen release (removal of  $\text{Li}_2\text{O}$ ) from the  $\text{Li}_2\text{MnO}_3$  ( $\text{Li}[\text{Li}_{1/3}\text{Mn}_{2/3}\text{O}_2]$ ) component. After this reaction, the  $\text{MnO}_2$ -like component is formed from  $\text{Li}_2\text{MnO}_3$ . During the second charge process, the sharp oxidation peak at around 4.5 V in the initial charge disappeared, which leads to the large irreversible capacity loss, and the oxidation peak at around 4.0 V shifts to ~3.9 V position, indicating that the bulk material structure and/or the electrode/electrolyte interface have been modified after the first cycle.

As shown in Fig. 6(a), there are two obvious oxidation peaks in the initial charge process, corresponding to the electrochemical reaction of  $\text{Ni}^{2+}$  to  $\text{Ni}^{4+}$  (cyan box in Fig. 6) and the removal of “ $\text{Li}_2\text{O}$ ” (black box in Fig. 6). After the first charge process, three distinct reduction peaks are observed at the range of (1) below 3.6 V, (2) 3.6–4.2 V and (3) above 4.2 V, corresponding to the reductions of (1)  $\text{Mn}^{4+/3+}$  (olive box in Fig. 6), (2)  $\text{Ni}^{4+/2+}$  and (3)  $\text{Co}^{4+/3+}$  (orange box (in the web version only) in Fig. 6). After the first cycle, the oxidation peak resulting from the removal of “ $\text{Li}_2\text{O}$ ” disappears. In the subsequent cycles, three distinct oxidation peaks are observed in charge processes at the range of (1) below 3.7 V, (2) 3.7–4.4 V and (3) above 4.4 V, corresponding to the  $\text{Mn}^{3+/4+}$  (magenta box in Fig. 6),  $\text{Ni}^{2+/4+}$  (cyan box in Fig. 6) and  $\text{Co}^{3+/4+}$  (wine box in Fig. 6) oxidations, respectively [27,38]. With the continuous cycle, the reduction and oxidation peaks of  $\text{Ni}^{2+/4+}$  and  $\text{Co}^{3+/4+}$  have no significant change. However, the reduction and oxidation peaks of  $\text{Mn}^{3+/4+}$  in the  $dQ_m/dV$  curves shift to the low

voltage region. The  $dQ_m/dV$  curves of the 20th, 30th and 50th cycle (shown in Fig. 6(e)–(g)) have a main peak at around 3.0 V in the discharge process. This peak can be ascribed to the reduction of  $\text{Mn}^{4+}$  to  $\text{Mn}^{3+}$  that may take place in the electrochemical reaction after the electrochemical activation of  $\text{Li}_2\text{MnO}_3$  component [25,39,40]. Reduction peaks below 3.0 V are attributed to the spinel-like phase. Thus, it can be deduced that the layered  $\text{LiMnO}_2$  phase transformed to the spinel-like phase during charge/discharge cycles. By comparison, the reduction peaks of HP-PVP sample do not shift to the low voltage region as critically as HP sample, shown in Figs. 5 and 6. It means that noticeable structural degradation of HP-PVP sample does not take place during the cycling process. At the same time, it can be seen from Fig. 6 that the  $\text{Mn}^{3+}/\text{Mn}^{4+}$  redox peak spacing of HP-PVP (the distance between two blue vertical) is smaller than HP (the distance between two red vertical) in the continuous cycling process. This suggests that HP-PVP has a better structural stability than HP. Meanwhile, due to the structural transformation, the  $\text{Mn}^{3+}/\text{Mn}^{4+}$  redox peak spacing of HP and HP-PVP become larger, meaning that the reversibility of both samples gets worse during the continuous cycle process.

In order to further evaluate the stability of the as-prepared samples, the cells were cycled applying a constant current density of  $25 \text{ mA g}^{-1}$  (~0.1 C rate) between 2.0 and 4.8 V at room temperature, as shown in Fig. 7. The entire as-prepared samples exhibit a similar cycle performance, with a gradual capacity fade to a constant. The capacity fade is attributed to the following two reasons: (i) the chemical instability of  $\text{Co}^{4+/3+}$  redox couple because of its overlap with the top of the  $\text{O}_2 2p$  band [41,42], and (ii) transformation from layered structured to spinel-like phase, which has been observed during cycling between 2.0 and 4.8 V [20,39]. The capacity retention of HP and HP-PVP are 84.4% and 84.1% after 50 cycles respectively, which are higher than P (78.9%) and SS (82.8%) samples and other researches [35,43]. At the same time, the HP-PVP cell shows a higher discharge capacity than HP cell.

Fig. 8 shows the SEM images of HP and HP-PVP samples after 50 cycles (charge and discharge @ 0.2 C). Compared with the original SEM images of the as-prepared samples (as shown in Fig. 2), the morphology of HP and HP-PVP samples has not been changed considerably after 50 cycles at 0.2 C. Hollow spherical particles are still visible (as shown in Fig. 8(a) and (c)), and the microstructure of HP (the quasi-sphere shaped particles, shown in Fig. 8(b)) and HP-PVP (the nanoplate-shaped particles, shown in Fig. 8(d)) can also be seen obviously. It means that the structure of HP and HP-PVP samples is very stable, which was not broken in the process of coating and charge–discharge cycling. The good cycle performances of HP and HP-PVP samples are probably due to the good layered structure (as shown in Fig. 1) and the stable hollow spherical structure.

To evaluate rate performance of the as-prepared cathode materials, the cells have been tested at various discharge rates of 0.1, 0.2, 0.5, 1 and 2 C between 2.0 V and 4.8 V, and the results are compared in Fig. 9. The charge/discharge efficiencies of the cathode materials at different rates are also shown in Fig. 9. HP and HP-PVP samples exhibit higher discharge capacities than P and SS samples. The discharge capacities of HP at 0.1, 0.2, 0.5, 1 and 2 C in the first cycle are 279.3, 259.4, 216.2, 192.6 and 147.1  $\text{mAh g}^{-1}$ , respectively. However, it decreases quickly in the following several cycles, especially at the large discharge rate. HP sample presents a considerable discharge capacity at 0.1 C and 0.2 C but serious capacity fades at high rates, and above 1 C it maintains only about 50% of that at 0.1 C. By comparison, HP-PVP sample has a higher discharge capacity and a better cycling stability than other samples at the same discharge rate, especially at the large discharge rate. It is due to the clearances supplied by the assembly of nanoplate-shaped particles. The clearances provide more interfaces for



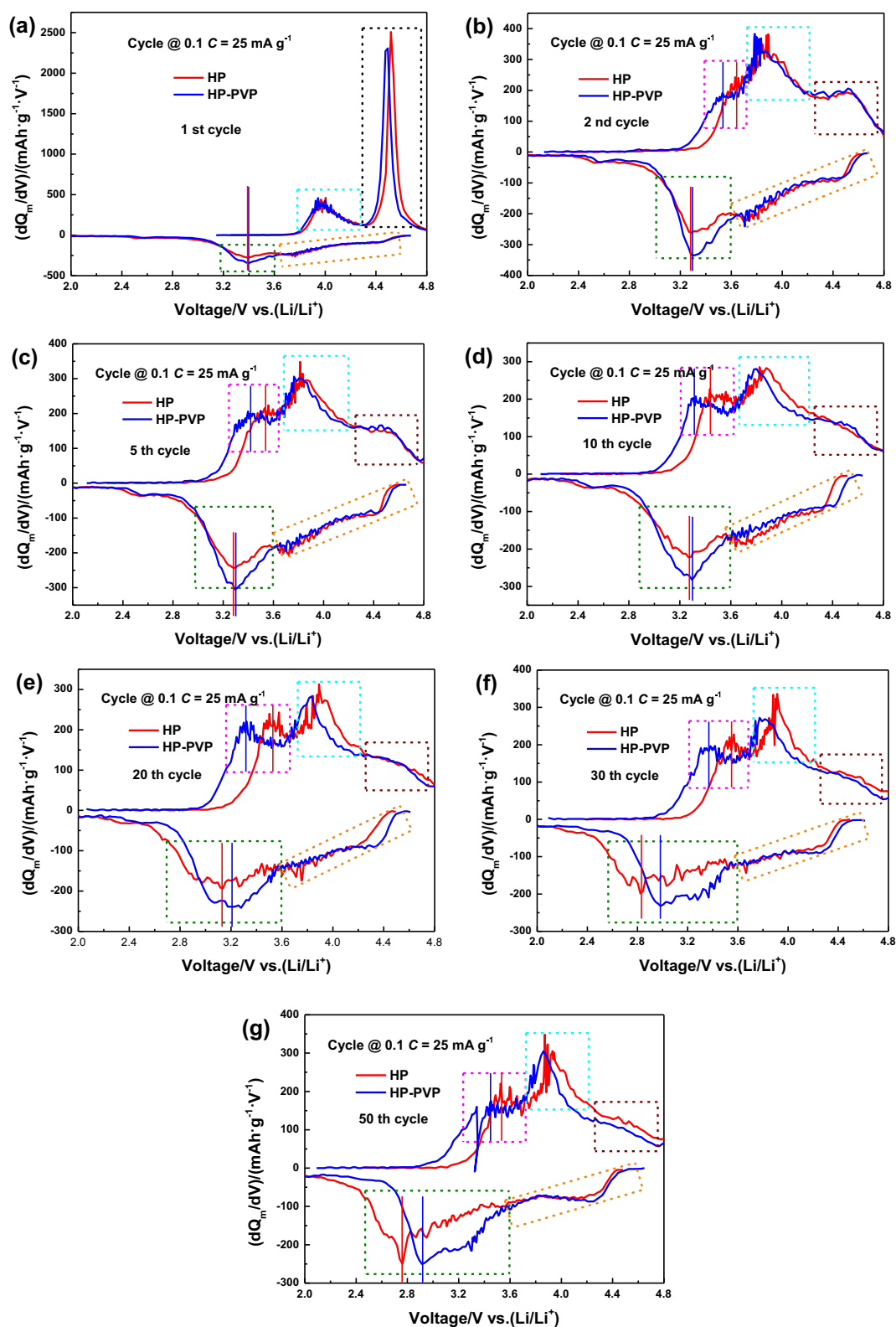
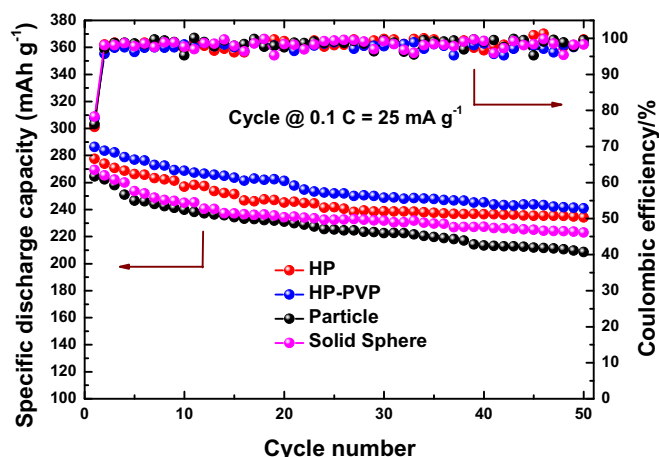


Fig. 6. The  $dQ_m/dV$  curves of the as-prepared samples at different cycle numbers at a constant current density of  $25 \text{ mA g}^{-1}$ .

active cathode materials and electrolyte, which shortens the transmission distance for  $\text{Li}^+$ . The results of BET test (HP:  $1.591 \text{ m}^2 \text{ g}^{-1}$ , HP-PVP:  $6.071 \text{ m}^2 \text{ g}^{-1}$ ) prove just this viewpoint above. This result clearly indicates that those hollow spheres assembled with nanoplate-shaped particles are responsible for the significant improvement of the rate and cycle performances.

Fig. 10 presents the charge–discharge voltage profiles of the samples at different discharge current density between 2.0 and 4.8 V at room temperature. Each cell was charged at a rate of 0.1 C and then discharged at different rates from 0.1 C to 2.0 C. As can be seen from Fig. 10, the discharge capacity of the HP-PVP sample is larger than the HP sample at every discharge rate. As the current



**Fig. 7.** Discharge capacities and efficiencies vs. the cycle number curves of the as-prepared samples at low current density ( $0.1\text{ C} = 25\text{ mA g}^{-1}$ ).

density increased from 0.1 C to 2.0 C, the discharge voltage plateau gradually declines. Compared with the profiles of the two samples in Fig. 10, the HP-PVP cell shows a more stable profile than HP cell. It can be due to the higher crystallinity, which is essential to obtain good electrochemical properties and to maintain its structural integrity during cycling, especially at high discharge current [33]. The shorter migration path of lithium is benefit for the rate performance and the stability of the discharge voltage plateau.

**Fig. 11** compares the cycling performances of HP, HP-PVP, P and SS electrodes at 1 C (The cells were cycled at 0.1 C in the first three cycles, and then cycled at 1.0 C). The initial discharge capacity at 1 C is 203.5, 197.7, 181.5 and 181 mAh g<sup>-1</sup> respectively. As shown in

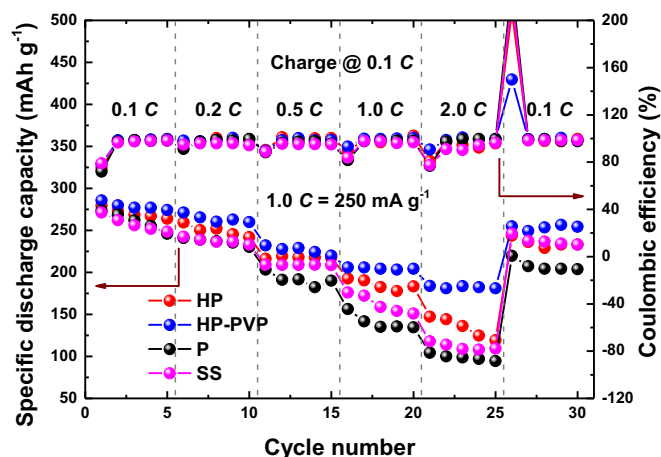


**Fig. 9.** The rate performances of the as-prepared samples at different discharge current densities.

Fig. 11, the capacities of HP, P and SS samples show a serious decrease, and then gradually stabilized at the subsequent cycles. Unlike the other samples, the capacity of HP-PVP sample shows a stable discharge capacity from the beginning. After 112 cycles at 1.0 C, the capacity retentions of HP, HP-PVP, P and SS samples are 58.9, 86.2, 57.4 and 28.1% respectively.

To gain a better understanding of factors leading to the differences in rate capabilities of the as-prepared samples, EIS measurements have been carried out on the four samples. EIS spectra of the samples and equivalent circuit are shown in Fig. 12.  $R_Q$  refers to the ohmic resistance between the working electrode and the reference electrode.  $R_S$  represents the resistance for lithium ion

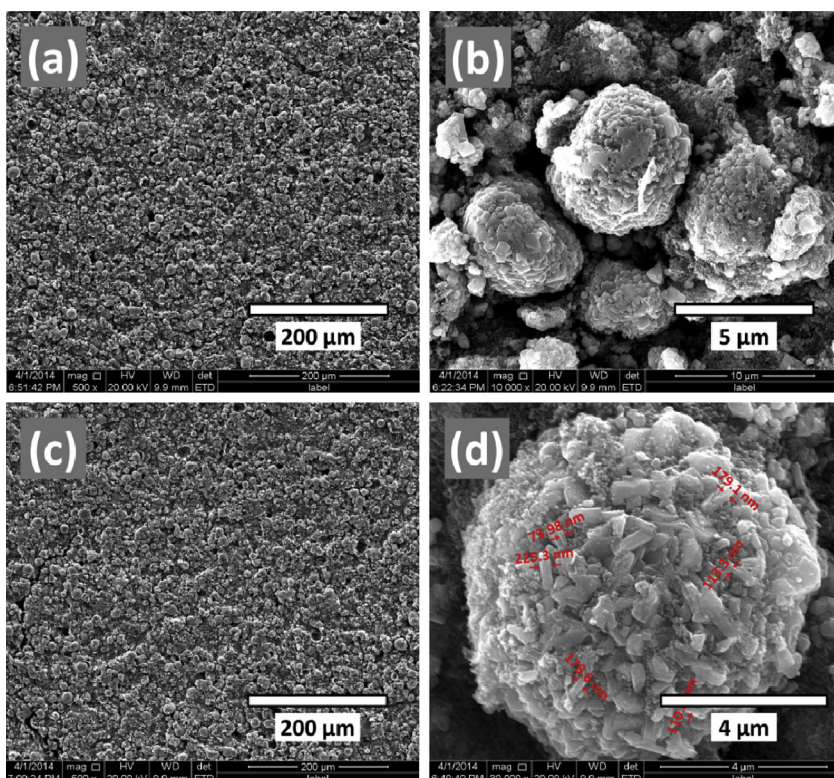


**Fig. 8.** SEM images of sample HP and HP-PVP after 50 cycles (charge and discharge @ 0.2 C): (a, b) HP, (c, d) HP-PVP. SEM images of sample HP and HP-PVP after 50 cycles (charge and discharge @ 0.2 C): (a, b) HP, (c, d) HP-PVP.



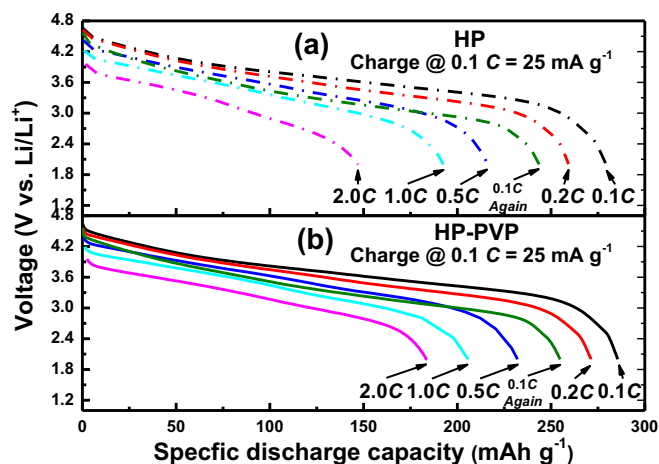


Fig. 10. The charge–discharge voltage profiles of the samples at different discharge current densities in the range from 2.0 to 4.8 V at room temperature.

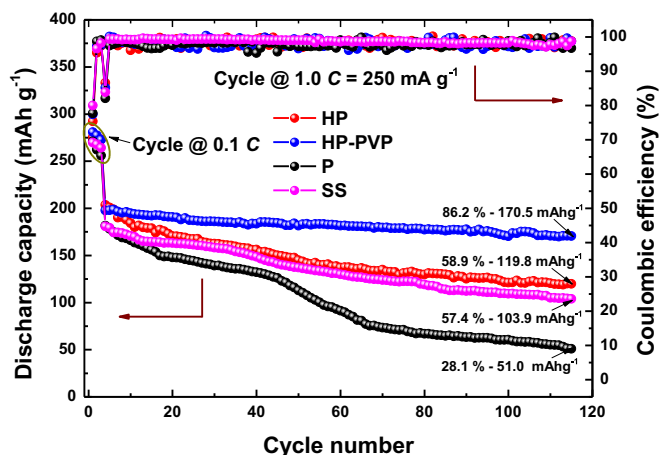


Fig. 11. The cycling performances of the as-prepared samples at a constant current density of  $1\text{ C} = 250\text{ mA g}^{-1}$ .

diffusion in the surface layer (SEI layer), which is indicated by the first semicircle (as shown in Fig. 12(b) at the high frequency region).  $R_{ct}$  refers to the charge transfer resistance, which is showed in the second semicircle (as shown in Fig. 12(b) at the medium-to-low frequency region). As it can be seen, the  $R_{\Omega}$  is negligible for all the as-prepared samples before and after the charge and discharge.

Table 3

The EIS values of the as-prepared samples.

Samples	Before cycle		After 50 cycles (charging to 4.2 V)		
	$R_{\Omega}$ ( $\Omega$ )	$R_{ct}$ ( $\Omega$ )	$R_{\Omega}$ ( $\Omega$ )	$R_s$ ( $\Omega$ )	$R_{ct}$ ( $\Omega$ )
HP	1.922	77.048	2.842	14.478	99.381
HP-PVP	2.311	55.139	2.325	5.030	57.505
P	2.382	160.168	2.663	10.067	162.174
SS	2.424	167.576	3.379	16.201	117.922

It is considered that the charge transfer process and lithium ion diffusion in the bulk materials could be the main factors in controlling the rate capability of materials. As shown in Fig. 12(a) and Table 3, HP-PVP has the smallest  $R_{ct}$  value. After 50 cycles, HP-PVP also has the smallest  $R_s$  and  $R_{ct}$  values (as shown in Fig. 12(b) and Table 3). The EIS results are corresponding to the rate performances for the as-prepared samples. The excellent rate performance of HP-PVP is attributed to the nanoplate-shaped particles and the clearances supplied by the assembly of these nanoplate-shaped particles, which shorten the migration path of lithium and enhance the specific area of the cathode materials.

#### 4. Conclusions

Two different kinds of hollow spherical materials  $\text{Li}_{1.2}\text{Mn}_{0.54}\text{Ni}_{0.13}\text{Co}_{0.13}\text{O}_2$  ( $0.5\text{Li}_2\text{MnO}_3 \cdot 0.5\text{LiNi}_{1/3}\text{Co}_{1/3}\text{Mn}_{1/3}\text{O}_2$ ), which assembled by the nanoplate-shaped particles (HP-PVP sample) and the quasi-sphere shaped particles (HP sample), were synthesized by homogeneous precipitation-hydrothermal synthesis. The high discharge capacity is due to the electrochemical activation of  $\text{Li}_2\text{MnO}_3$ , which makes Mn (in  $\text{Li}_2\text{MnO}_3$ ) work in the subsequent cycles. In the initial charge process,  $\text{Li}_2\text{MnO}_3$  is activated to form  $\text{MnO}_2$ -like component with the removal of “ $\text{Li}_2\text{O}$ ”, and then the  $\text{MnO}_2$ -like component is transformed into layered  $\text{LiMnO}_2$  in the initial discharge process. The crystallinity and layered structure are very important factors for the electrochemical properties and the structural integrity during cycling. The HP-PVP sample has a better crystallinity, layered structure and higher surface area (due to lots of clearances). It exhibits better electrochemical properties than the HP sample, especially at the high discharge current. After 112 cycles at  $1.0\text{ C}$ , HP-PVP has a high discharge capacity of  $170.5\text{ mAh g}^{-1}$ , with capacity retention of 86.2%. It is due to the lots of clearances generated in the assemble processes of nanoplate-shaped particles to the hollow spheres, which shorten the transmission distance for  $\text{Li}^+$  from the cathode materials to electrolyte. The hollow spherical structure is beneficial to improve the rate performance of lithium-rich cathode materials.

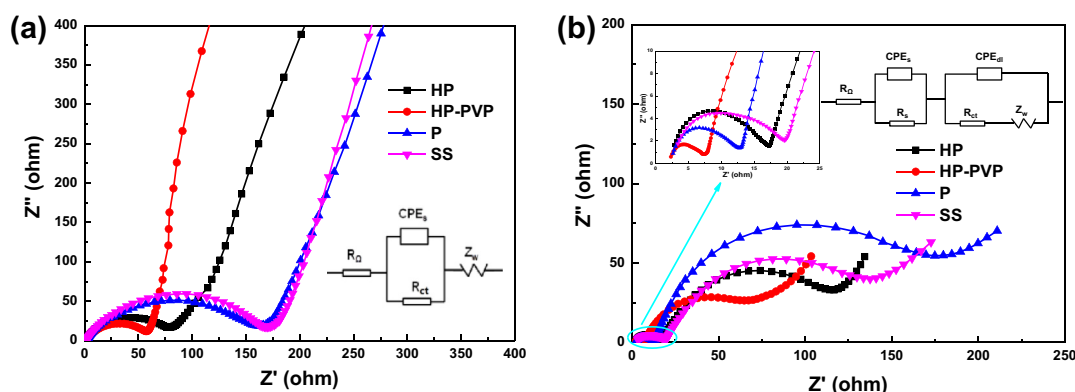


Fig. 12. EIS spectra of  $\text{Li/Li}[\text{Li}_{0.2}\text{Mn}_{0.54}\text{Ni}_{0.13}\text{Co}_{0.13}]\text{O}_2$  cells of the as-prepared samples: (a) before cycle, (b) after 50 cycles, then charge to 4.2 V.

## Acknowledgments

This work was funded by the Key National Basic Research and Development Program of China (2009CB220100), National Natural Science Foundation of China (51102018, 21103011), Program for New Century Excellent Talents in University (NCET-13-0044), BIT Scientific and Technological Innovation Project (2013CX01003) and Science Program of the State Grid Corporation of China (DG71-13-007).

## References

- [1] J.-L. Liu, J. Wang, Y.-Y. Xia, *Electrochim. Acta* 56 (2011) 7392–7396.
- [2] R. Santhanam, B. Rambabu, *J. Power Sources* 195 (2010) 5442–5451.
- [3] P.N. Kumta, D. Gallet, A. Waghay, G.E. Blomgren, M.P. Setter, *J. Power Sources* 72 (1998) 91–98.
- [4] T. Ohuzuku, A. Ueda, M. Nagayama, *J. Electrochem. Soc.* 140 (1993) 1862–1870.
- [5] T.-J. Kima, D. Son, J. Cho, B. Park, *J. Power Sources* 154 (2006) 268–272.
- [6] L. Xiao, Y. Guo, D. Qu, B. Deng, H. Liu, D. Tang, *J. Power Sources* 225 (2013) 286–292.
- [7] N.D. Trinh, M. Saulnier, D. Lepage, S.B. Schougaard, *J. Power Sources* 221 (2013) 284–289.
- [8] F. Wu, M. Wang, Y. Su, L. Bao, S. Chen, *J. Power Sources* 195 (2010) 2362–2367.
- [9] F. Wu, Z. Wang, Y. Su, N. Y. L. Bao, S. Chen, *J. Power Sources* 247 (2014) 20–25.
- [10] S.-H. Park, Y.-K. Sun, *J. Power Sources* 119–121 (2003) 161–165.
- [11] L. Zhang, T. Muta, H. Noguchi, X. Wang, M. Zhou, M. Yoshio, *J. Power Sources* 117 (2003) 137–142.
- [12] Y.J. Park, M.G. Kim, Y.-S. Hong, X. Wu, K.S. Ryu, S.H. Chang, *Solid State Commun.* 127 (2003) 509–514.
- [13] L. Yu, W. Qiu, J. Huang, F. Lian, *Int. J. Min. Metal. Mater.* 16 (2009) 458–462.
- [14] X. Zhao, Y. Cui, L. Xiao, H. Liang, H. Liu, *Solid State Ionics* 192 (2011) 321–325.
- [15] M.G. Kim, M. Jo, Y.-S. Hong, J. Cho, *Chem. Commun.* (2009) 218–220.
- [16] Q. Peng, Z. Tang, L. Zhang, X. Liu, *Mater. Res. Bull.* 44 (2009) 2147–2151.
- [17] D. Kim, S.-H. Kang, M. Balasubramanian, C.S. Johnson, *Electrochem. Commun.* 12 (2010) 1618–1621.
- [18] J. Zhang, X. Guo, S. Yao, W. Zhu, X. Qiu, *J. Power Sources* 238 (2013) 245–250.
- [19] W.-H. Ryu, S.-J. Lim, W.-K. Kim, H.S. Kwon, *J. Power Sources* 257 (2014) 186–191.
- [20] X. Liu, J. Liu, T. Huang, A. Yu, *Electrochim. Acta* 109 (2013) 52–58.
- [21] Y. Wu, A. Manthiram, *Electrochem. Solid-State Lett.* 9 (2006) A221–A224.
- [22] Q.Y. Wang, J. Liu, A.V. Murugan, A. Manthiram, *J. Mater. Chem.* 19 (2009) 4965–4972.
- [23] Y. Wu, J. Ming, L. Zhuo, Y. Yu, F. Zhao, *Electrochim. Acta* 113 (2013) 54–62.
- [24] S.J. Shi, J.P. Tu, Y.Y. Tang, Y.Q. Zhang, X.L. Wang, C.D. Gu, *J. Power Sources* 240 (2013) 140–148.
- [25] M.M. Thackeray, S.H. Kang, C.S. Johnson, J.T. Vaughey, R. Benedek, S.A. Hackney, *J. Mater. Chem.* 17 (2007) 3112–3125.
- [26] Z. Lu, J.R. Dahn, *J. Electrochem. Soc.* 150 (2003) A1044–A1051.
- [27] K.M. Shaju, G.V. Subba Rao, B.V.R. Chowdari, *Electrochim. Acta* 48 (2002) 145–151.
- [28] H.A.M. Abuzeid, A.M.A. Hashem, A.E. Abdel-Ghany, A.E. Eid, A. Mauger, H. Groult, C.M. Julien, *J. Power Sources* 196 (2011) 6440–6448.
- [29] J. Li, R. Klöpsch, M.C. Stan, S. Nowak, M. Kunze, M. Winter, S. Passerini, *J. Power Sources* 196 (2011) 4821–4825.
- [30] F. Fu, G.-L. Xu, Q. Wang, Y.-P. Deng, X. Li, J.-T. Li, L. Huang, S.-G. Sun, *J. Mater. Chem. A* 1 (2013) 3860–3864.
- [31] X.W. Lou, D. Deng, J.Y. Lee, J. Feng, L.A. Archer, *Adv. Mater.* 20 (2008) 258–262.
- [32] Y.H. Min, G.D. Moon, B.S. Kim, B.K. Lim, J.S. Kim, C.Y. Kang, U.Y. Jeong, *J. Am. Chem. Soc.* 134 (2012) 2872–2875.
- [33] A.R. Armstrong, M. Holzapfel, P. Novak, C.S. Johnson, S. Kang, M.M. Thackeray, P.G. Bruce, *J. Am. Chem. Soc.* 128 (2006) 8694–8698.
- [34] J. Liu, Q. Wang, B. Reeja-Jayan, A. Manthiram, *Electrochem. Commun.* 12 (2010) 750–753.
- [35] X.-J. Guo, Y.-X. Li, M. Zheng, J.-M. Zheng, J. Li, Z.-L. Gong, Y. Yang, *J. Power Sources* 184 (2008) 414–419.
- [36] Z. Lu, J.R. Dahn, *J. Electrochem. Soc.* 149 (2002) A815–A822.
- [37] M.M. Thackeray, *J. Electrochem. Soc.* 142 (1995) 2558–2563.
- [38] N. Yabuuchi, Y. Makimura, T. Ohzuku, *J. Electrochem. Soc.* 154 (2007) A314–A321.
- [39] C.S. Johnson, N.C. Li, C. Lefief, J.T. Vaughey, M.M. Thackeray, *Chem. Mater.* 20 (2008) 6095–6106.
- [40] F. Amalraj, D. Kovacheva, M. Talianker, L. Zeiri, J. Grinblat, N. Leifer, G. Goobes, B. Markovsky, D. Aurbach, *J. Electrochem. Soc.* 157 (2010) A1121–A1130.
- [41] J. Choi, A. Manthiram, *Solid State Ionics* 176 (2005) 2251–2256.
- [42] R.V. Chebiam, F. Prado, A. Manthiram, *Chem. Mater.* 13 (2001) 2951–2957.
- [43] J.M. Zheng, J. Li, Z.R. Zhang, X.J. Guo, Y. Yang, *Solid State Ionics* 179 (2008) 1794–1799.